Expansion of C4 vegetation and wildfire intensification during the late Cenozoic caused atmospheric CO2 drawdown

Prosenjit Ghosh (pghosh@iisc.ac.in)
Indian Institute of Science

Thamizharasan S
Indian Institute of Science

Nisha Nair
National Centre for Polar and Ocean Research

Physical Sciences - Article

Keywords:

Posted Date: April 25th, 2022

DOI: https://doi.org/10.21203/rs.3.rs-1583189/v1

Expansion of C_4 vegetation and wildfire intensification during the late Cenozoic caused atmospheric CO_2 drawdown

Thamizharasan S[1,2], Prosenjit Ghosh[1,2*], Nisha Nair[3]

[1]Centre for Earth Sciences, Indian Institute of Science; Bangalore – 560012

[2]Divecha Centre for Climate Change, Indian Institute of Science; Bangalore – 560012

[3]Geosciences, National Centre for Polar and Ocean Research; Vasco-da-Gama, Goa-403 804

*Corresponding author. Email: pghosh@iisc.ac.in

Abstract:

The late Cenozoic [6.8 to 0.5 Ma] vegetation ecosystem preferred to hatch slack photosynthetic C_4 pathways[1,2] and witnessed intense wildfire activity[3–5]. Modern-day such ecosystems are considered as potential atmospheric CO_2 pumps due to their ability to enhance erosion rate and rapid burial of charcoal of terrestrial origin [6–8]. However, their role has never been considered in the context of the Late Cenozoic CO_2 drawdown. Here, we showed evidence of C_4 vegetation expansion, intense wildfire activities, and consequent shift in the soil erosion rate during Late Cenozoic based on terrestrial organic carbon (TOC) stable isotope, clay fixed ammonium stable nitrogen isotope, and its mean accumulation rate (MAR) from the sediments of International Ocean Discovery Program (IODP) expedition 362 site U1480, Nicobar fan. Our result suggests that the Plio-Pleistocene boundary ecosystem recorded 22% more C_4 vegetation and 2.5 times more wildfire-associated erosion rate than the Late Miocene. We exhibit the yield of both processes on ~150ppm drop-in pCO2 during the Plio-Pleistocene boundary through an 11% rise in silicate mineral reactivity and 2.3 times terrestrial organic carbon burial. These estimates are based on a reappraisal of global seawater $^{87}Sr/^{86}Sr$ ratio and TOC MAR at the present study site. Overall, our results demonstrate that C_4 vegetational expansion and wildfire are likely to function in silicate mineral reactivity and terrestrial organic burial during Late Cenozoic. We

anticipate our results serve as a premise for further investigations into the linkage between global wildfire occurrences in driving C_4 vegetational abundances and climate change.

Main text:

Late Cenozoic drop in the partial pressure of atmospheric CO_2 (pCO_2) is attributed to the increased erosion rate[9–11] and burial of terrestrial derived organic matter[12]. However, the driving mechanism for these processes is still poorly understood. Concurrently, the preference of hatch slack photosynthetic C_4 vegetation at the expense of the C_3 photosynthetic pathway happened worldwide[1,2]. C_4 vegetation is supported in a fine crumb clod texture mollisols whose internal surface area is larger than the coarse blocky textured soils hosting C_3 vegetation[6,13], which facilitate ten times excess carbon fixation by C_4 vegetation-associated soil than forestland in the comparable climate regime[14]. The C_4 vegetation is susceptible to wildfire and can recover quickly after each fire event [15,16]. The recurrent wildfire activities are attributed as a significant contributor to atmospheric CO_2 globally at an interannual time scale but compensated by the drawdown of CO_2 due to plant regrowth[8]. Further, Wildfires sequestrate atmospheric CO_2 by producing 256 Tg C of charcoal annually[8] and promoting soil erosion[7]. Charcoal can be stockpiled in a terrestrial and marine system for centuries to millennia and can be contemplated as a long-term effective mechanism for carbon sequestration. We proposed here an effective method for locking atmospheric carbon by expansion of C_4 vegetation and high intense event of wildfire activities in the flood plain region of Himalayan river basin during the Late Cenozoic.

Modern-day Himalayan rivers, especially Ganges-Brahmaputra, supply 24% of sediments[17], which includes 10-20% of organic carbon of terrestrial origin to the global ocean[18] and participate in regulation of the atmospheric CO_2 levels. These sediments are brought by rivers to the Bengal-Nicobar fan and develop a continuous record of sedimentation documenting shift

in climate and ecology over flood plain region of South Asia. The previous record of vegetational shift[2,19], wildfire intensity[5] and erosion rate[9] over South Asia during Late Cenozoic were reported from the region of Bengal fan. A recent expedition of the International Ocean Discovery Program (IODP) 362 sampled and logged the sedimentary record from the Nicobar fan. The detrital zircon age spectra[20] and radiogenic Sr and Nd isotope composition[21] of turbidite deposits from IODP 362 site U1480 suggest that the Eastern Himalaya and Indo-Burma range are major sediment sources. The biostratigraphy and magnetostratigraphy datums based age-depth model suggests the Nicobar fan received nearly 400% excess sediment from river draining South East Asia than the proportion accumulated at the Bengal fan during late Cenozoic [20,22]. Together with this, the presence of wood remains from the terrestrial plants, and the low calcium carbonate content of sediments confirms the exclusive dominance of land-derived sediments with insignificant input from primary marine productivity at the site of deposition[23,24]. These features make the Nicobar fan an archetypal for examining the factors responsible for C_4 vegetation and ascertaining the link with intense wildfire events, driving rapid CO_2 sequestration trends detected in the Late Cenozoic sedimentary record.

Here we reconstructed proportional shift in C_4 vegetation (%), wildfire intensity, and coupled erosion rate over the region of Eastern Himalaya and Indo-Burma using stable carbon $\{\delta^{13}C_{TOC} = [(^{13}C/^{12}C_{TOC})/(^{13}C/^{12}C_{VPDB}) - 1] * 1000\}$ of Total Organic Carbon (TOC), and nitrogen isotope $\{\delta^{15}N_{f.\ NH_4^+} = [(^{15}N/^{14}N_{f.NH_4^+})/(^{15}N/^{14}N_{N_2\ air}) - 1] * 1000\}$ and Mean Accumulation Rate (MAR) of fixed ammonium in clay from Late Cenozoic [6.8 to 0.5 Ma] sedimentary succession of IODP 362 site U1480. Furthermore, we showed coupling of C_4 vegetational shift and increased erosion rate on the regulation of mineral reactivity and consequent burial of terrestrial organic matter through a reappraisal of global seawater $^{87}Sr/^{86}Sr$ ratio and TOC MAR at the site of the present study.

Late Cenozoic C_4 expansion on Eastern Himalaya and Indo-Burma Range:

Isotopic composition of organic matter ($\delta^{13}C_{TOC}$ value) ranges between -32.1‰ VPDB and -15.8‰ VPDB (Fig. 1a & **Error! Reference source not found.**), which implies variable contribution from C_3 and C_4 vegetations present in the catchment. These isotope values are converted in terms of fraction of C_4 vegetation-derived carbon by assuming a binary mixing model with a well-defined $\delta^{13}C$ values for the modern-day C_3 and C_4 plant present in South Asia. The prescribed region specific $\delta^{13}C$ values for C_3 and C_4 vegetation are -32.6‰ and -10.4‰, respectively[25]. Our estimates show C_4 vegetation was present in the catchment with fractional percentage of ~25 ± 3% (n=17) during Late Miocene (6.8 to 5.2 Ma) (Fig. 1a). This is substantiated with reconstructed C_4 vegetation record over the region of Indo-Burma based on $\delta^{13}C$ of mammals tooth enamel[26] and dominance of deciduous forest in the expense of wetland evergreen vegetation over Eastern Himalaya[27]. Afterward, the percentage dominance of C_4 vegetation started growing and reached maximum value of ~47 ± 2% (n=31) at Plio-Pleistocene boundary (3.0 to 1.8 Ma) (Fig. 1a). These two stages registering expansion of C_4 vegetation during Late Cenozoic are global in nature and found in several regions across many continents[2]. However, factors responsible for the vegetational shift is highly debatable with argument supporting appropriate pCO_2 level[28], increased aridity[29,30] and intense wildfire activity[4,5]. While the earlier two factors are respectively contested by fossilised C_4 grass pollen record[1] and stable hydrogen isotope of leaf wax[31], sufficient evidence favoured wildfire intensity as the only option promoting C_4 vegetation[3–6].

Proxy for wildfire intensity and associated erosion rate:

Wildfire is adjudged as a possible mechanism to explain the late Cenozoic proliferation of C_4 vegetation based on the modern-day analogy[3,5,15]. Wildfire generates tropospheric ozone, which is toxic to plant productivity[32]. The waning of productivity by Wildfire increases the soil temperature and moisture, thereby significantly accelerating the soil ammonification rate and reducing plant NH_4^+ uptake, making the soil environment excess in NH_4^+ radical[33]. This

process enriches lighter isotope of nitrogen(^{14}N) in soil ammonium[34]. Due to similar ionic radii and low hydration energy, NH_4^+ in the soil can replace K^+ in the interlayer structure of clay minerals[35]. The penetration of NH_4^+ into the clay mineral interlayer reduces the interlayer distance by 1nm and traps NH_4^+ in silicate structure as fixed NH_4^+.

On the note of clay-fixed NH_4^+ concentration, the competition between soil erosion and leaching plays a significant role. The leaching process can reduce soil NH_4^+ content via the process of dissolution with water from runoff and groundwater interaction. This will allow diffusion of clay-fixed NH_4^+ to attain chemical equilibrium with vicinity soil ammonium[33]. Such diffusion can be avoided by quick transport of clay from the place of origin to the adjoining lowland area. These characteristics make the stable nitrogen isotope ($\delta^{15}N_{f.\ NH_4^+}$) and fixed NH_4^+ in the clays as a unique proxy for wildfire intensity and soil erosion rate, respectively.

Wildfire intensity and triggering mechanism:

The absence of fixed NH_4^+ in the clays deposited during the time window of 6.8 to 6.3Ma revealed a period without wildfire activity in the river's catchment. With progressive younging up in the strata, $\delta^{15}N_{f.NH_4^+}$ values varied between -6.5‰ and +4.5 (Fig. 1c & **Error! Reference source not found.**). The $\delta^{15}N_{f.\ NH_4^+}$ denotes a net effect of ammonium mineralization and ammonium assimilation by the plants. The organic nitrogen pool in the soil (N_s) is enormous and undergoes infinitesimal change due to the mineralized NH_4^+ pool generated after the Wildfire. We considered the ammonium mineralization process a zero-order reaction based on modern-day observation from the Wildfire experiencing chaparral soil of California[36], which contains 10 to 5mg/g of organic nitrogen compared to about 2.37 to 2.48 μg/g of NH_4^+. Then, the post-wildfire mineralized NH_4^+ ($\delta^{15}N_{NH_4^+(initial)}$) is mostly consumed by the process of assimilation rather than nitrification[37–39]. Therefore, the plants' ammonium assimilation

124 governs the soil $\delta^{15}N_{NH_4^+}$. This ammonium assimilation imparts large isotopic fractionation
125 ($\varepsilon^{15}_{plants-soil.NH_4^+} = \delta^{15}N_{plants} - \delta^{15}N_{soil.NH_4^+}$) of -10.2 ± 7.9‰[34]. We converted our
126 $\delta^{15}N_{f.\ NH_4^+}$ record to the fractional percentage of soil NH_4^+ assimilated by plants using the
127 steady-state isotope model.

128 $$f_{Plants\ NH_4^+\ assimilation} = \frac{\delta^{15}N_{soil.NH_4^+(initial)} - \delta^{15}N_{soil.NH_4^+(remaining)}}{\varepsilon^{15}_{plants-soil.NH_4^+}}$$

129 $$\delta^{15}N_{soil.NH_4^+(remaining)} = \delta^{15}N_{f.\ NH_4^+}$$

130

131 We assigned lightest $\delta^{15}N_{f.\ NH_4^+}$ value as $\delta^{15}N_{soil.NH_4^+(initial)}$ and estimated fraction of soil
132 NH_4^+ assimilated by the plant population. This is with the assumption that the lightest
133 $\delta^{15}N_{f.\ NH_4^+}$ reflects absence of soil NH_4^+ assimilation by plant ecosystem. The low nutrient
134 uptake value was prescribed over the time interval 6 to 4.9 Ma with a mean ± 1SE value of 42
135 ± 13% (n=6) and similarly, in the time interval 2.6 to 1.8 Ma with the mean ± 1SE value of 43
136 ± 5% (n=14) (Fig. 1c). These intervals are unequivocally registered intense wildfire
137 activity and contemporaneous with evident from the independent record of Wildfire across the
138 globe [4,5,40,41].
139 The most widely accepted Late Cenozoic wildfire triggering mechanism is increased
140 monsoonal seasonality [3,5]. More recently, an increase in cosmic ray flux due to nearby
141 supernova explosion is proposed as a most possible mechanism to induce anomalous lightning
142 and thunderstorm activities during the Late Cenozoic, attributed as a cause for widespread
143 wildfire[42]. The seasonal monsoon precipitation drives the terrestrial productivity during the wet
144 season and converted into highly combustible fuel biomass. The cosmic ray (high energy
145 proton and other nuclei) cause frequent lightning activities; which spark Wildfire in a
146 deciduous and evergreen forest[43]. Monsoonal seasonality in the Late Cenozoic as a factor for
147 wildfire activity during the dry time in the tropics[6], but fails to explain events of wildfire

activity in the Arctic during the nearly same period [41]. A global scenario of nearby supernova explosion inducing widespread wildfire occurrences due to frequent lighting activities can explain the C_4 expansion and climatic transformation during the late Cenozoic. The observation of the decay corrected abundances of Iron-60 (^{60}Fe) incorporation in Ferromanganese crust[44] suggests intense cosmic ray shower due to the explosion of nearby supernova coincides with the late Cenozoic wildfire events(Fig. 1b).

Wildfire linked Erosion rate:

The fixed clay NH_4^+MAR estimated here serves as a proxy for the erosion rate and varies between 1 and 49.5 g/cm^2/Myr during the Late Cenozoic (Fig. 1d & **Error! Reference source not found.**). The fixed NH_4^+MAR (Mean ± 1SE) estimates during Late Miocene (6.3 to 6 Ma) and Plio-Pleistocene (2.3 Ma to 1.9 Ma) time was defined using multiple samples with the mean value of 10.7±1.7 g/cm^2/Myr (n=5) and 26.3±4.2 g/cm^2/Myr (n=11) respectively. The increment of erosion rate by 2.5 times is observed during the Plio-Pleistocene compared to Late Miocene. Such growth in fixed clay NH_4^+MAR during Plio-Pleistocene was also reported over the Pacific ocean [45]. In addition, independent validation of erosion rate shift is available from other proxies, such as the magnetic susceptibility index of the sedimentary package from our study location and decay corrected ^{10}Be concentration-based erosion rate evaluation from central Asia (Extended Data Fig 1). Observed amplification of erosion rate can also be addressed by incorporating rapid tectonics[9,10] and glacial reworking[11] processes. However, the low-temperature thermochronometers from continental sedimentary archives suggests tectonism and glacial retreat caused insignificant change in the erosion rate during Late Cenozoic[46]. We proposed here that intensifying wildfire activity during Late Miocene and Plio-Pleistocene boundary is a potential driver for enhanced erosion rate and allowing the rapid burial of organic matter from terrains dominated by the C_4 vegetation.

Erosion implication on atmospheric CO_2 sequestration:

Erosion usually subjects reactive/fresh minerals to the weathering process and transports organic matter from the continent to the adjacent basin for burial [13,18]. These mechanisms allow rapid sequestration of atmospheric CO_2 and are registered in the sedimentary proxy record (Fig. 1g). The seawater $^{87}Sr/^{86}Sr$ record displays two stages of increase in radiogenic Sr in the time interval 7Ma to 4Ma and 2.5Ma to a modern-day and intermittent state of nearly constant values (Extended Data Fig. 3). The seawater $^{87}Sr/^{86}Sr$ is recorder of $^{87}Sr/^{86}Sr$ ratio and Sr flux from the river runoff and hydrothermal input from fluids generated in the Mid Oceanic Ridges. The hydrothermal Sr flux and $^{87}Sr/^{86}Sr$ ratio are governed by the seafloor spreading rate and $^{87}Sr/^{86}Sr$ of magmatic fluid at Mid Oceanic Ridges. These ratios were constant during Late Cenozoic [47,48]; encompassing the period of the present study. The $^{10}Be/^{9}Be$ ratio of seawater was constant and indicative of constant weathering flux[49]. Therefore the $^{87}Sr/^{86}Sr$ ratio recorded in Late Cenozoic seawater is indication of riverine $^{87}Sr/^{86}Sr$ ratio. This is also substantiated by the $^{87}Sr/^{86}Sr$ record in the pedogenic clay from Bengal fan[50] and pedogenic carbonate from lowland sediments of Himalayan foreland [51].

Modern-day, the Himalayan-Tibetan Plateau (HTP) river solely contribute ~23.3% of Sr flux to the Ocean [48]. If we held the rest of river $^{87}Sr/^{86}Sr$ ratio at modern value, the reconstructed $^{87}Sr/^{86}Sr$ ratio of HTP river suggests 0.0014 rise during Late Cenozoic (Fig. 1f). This rise can be accounted by evolution of ^{87}Rb decay and increased reactivity of mineral with high $^{87}Sr/^{86}Sr$ ratio in the parent rock. The Sr and Nd isotopic composition of sediments from Bengal and Nicobar fun suggests major contribution from Higher Himalayan Crystalline Series (HHCS) [21,50]. The HHCS consists of meta-sedimentary rocks ($^{87}Sr/^{86}Sr = 0.7646 \pm 0.0391$) and Anatectic granites ($^{87}Sr/^{86}Sr = 0.7600 \pm 0.0142$) that extends from Assam to Pakistan[52]. The estimated change in $^{87}Sr/^{86}Sr$ ratio due to excess radioactive decay of ^{87}Rb during Late Cenozoic, is inferred using modern-day value of $^{87}Sr/^{86}Sr$ and $^{87}Rb/^{86}Sr$, for meta-sedimentary rock and

Anatectic granite are 0.0001 and 0.0004, respectively. This variation solely cannot explain the increment in the riverine $^{87}Sr/^{86}Sr$ without involving increased reactivity of minerals with a high $^{87}Sr/^{86}Sr$ ratio. We estimated mineral reactivity in terms of reaction rate (k) of ^{87}Sr dissolution (& hence $^{87}Sr/^{86}Sr$), assuming first-order kinetics for the time interval 7 Ma to 4 Ma and 2.5 Ma to modern-day. The estimated k (Fig. 1f) value for the time interval 7Ma to 4Ma is 3.17×10^{-4} Myr^{-1} (~31.5 m.y. is required to increase the riverine ^{87}Sr by 1%) and rise to 3.51×10^{-4} $Myr^{-1}$for the time interval 2.5 Ma to modern-day (accordingly ~28.5 m.y. time will be required to increase the riverine ^{87}Sr by 1%).

Another consequence of increased erosion is the rapid organic carbon burial in proximal basins. Further, the C_4 vegetational expansion in the Late Cenozoic can also contribute high organic carbon, given that C_4 vegetation is supported by mollisols, which has the potential to hold ten times more organic carbon than coarse-grained soil found for C_3 vegetation in a comparable climate zone [6]. We estimated the burial of organic carbon using TOC MAR values. The high value of TOC MAR (Mean ± 1SE) was noted during the Late Miocene time interval (6.5 to 6 Ma) and Plio-Pleistocene time interval (2.4 to 1.8 Ma) with 51±6 $g/cm^2/Ma$ (n=11) and 117 ± 12 $g/cm^2/Ma$ (n=20) respectively (Fig. 1e & **Error! Reference source not found.**) defining the abundances. The shift in the TOC MAR values was in-phase with erosion rate proxy and C_4 expansion trend, providing for the first time a new mechanism of rapid CO_2 suction from the atmosphere and the role of nature-based terrestrial vegetation management scenario in late Cenozoic settings over the region of Eastern Himalaya and Indo-Burma.

Conclusion:

Overall, the present study elucidates the role of C_4 vegetation and associated Wildfire in the increment of erosion rate and rapid drawdown of CO_2 from the global atmosphere during the Late Cenozoic. Compared to Late Miocene, the Plio-Pleistocene boundary recorded 22% more C_4 vegetation and 2.5 times more wildfire-associated erosion rate. Both processes yielded a

~150ppm drop-in pCO_2 through an 11% rise in silicate mineral reactivity and 2.3 times organic carbon burial. Given that the 24% global terrestrial sediment flux and 10 to 20% of terrestrial organic carbon are depositing in Bengal and Nicobar fan[17,18], our study provides insight into the C_3 to C_4 vegetational shift associated with wildfire activity is effective in global environmental transformation during Late Cenozoic. The results may serve as a premise for further investigations into the linkage between C_4 vegetational abundance, Wildfire, and climate change.

References:

1. Edwards, E. J. *et al.* The origins of C4 Grasslands: Integrating evolutionary and ecosystem science. *Science (80-.).* **328**, 587–591 (2010).

2. Dunlea, A., Giosan, L. & Huang, Y. Pliocene expansion of C4 vegetation in the Core Monsoon Zone on the Indian Peninsula. *Clim. Past Discuss.* **2**, 1–17 (2020).

3. Keeley, J. E. & Rundel, P. W. Fire and the Miocene expansion of C4 grasslands. *Ecol. Lett.* **8**, 683–690 (2005).

4. Karp, A. T., Behrensmeyer, A. K. & Freeman, K. H. Grassland fire ecology has roots in the late Miocene. *Proc. Natl. Acad. Sci. U. S. A.* **115**, 12130–12135 (2018).

5. Karp, A. T., Uno, K. T., Polissar, P. J. & Freeman, K. H. Late Miocene C4 Grassland Fire Feedbacks on the Indian Subcontinent. *Paleoceanogr. Paleoclimatology* **36**, 1–20 (2021).

6. Retallack, G. J. Cenozoic expansion of grasslands and climatic cooling. *J. Geol.* **109**, 407–426 (2001).

7. Johansen, M. P., Hakonson, T. E. & Breshears, D. D. Post-fire runoff and erosion from rainfall simulation: Contrasting forests with shrublands and grasslands. *Hydrol.*

Process. **15**, 2953–2965 (2001).

8. Jones, M. W., Santín, C., van der Werf, G. R. & Doerr, S. H. Global fire emissions buffered by the production of pyrogenic carbon. *Nat. Geosci.* **12**, 742–747 (2019).

9. Rea, D. K. Delivery of Himalayan sediment to the northern Indian Ocean and its relation to global climate, sea level, uplift and seawater strontium. *Geophys. Monogr.* **70**, 387–402 (1992).

10. Peizhen, Z., Molnar, P. & Downs, W. R. Increased sedimentation rates and grain sizes 2-4 Myr ago due to the influence of climate change on erosion rates. *Nature* **410**, 891–897 (2001).

11. Herman, F. *et al.* Worldwide acceleration of mountain erosion under a cooling climate. *Nature* **504**, 423–426 (2013).

12. France-Lanord, C. & Derry, L. A. Organic carbon burial forcing of the carbon cycle from himalayan erosion. *Nature* **390**, 65–67 (1997).

13. Chadwick, O. A., Kelly, E. F., Merritts, D. M. & Amundson, R. G. Carbon dioxide consumption during soil development. *Biogeochemistry* **24**, 115–127 (1994).

14. Stallard, R. F. Terrestrial sedimentation and the carbon cycle: Coupling weathering and erosion to carbon burial. *Global Biogeochem. Cycles* **12**, 231–257 (1998).

15. Flores, B. M. & Holmgren, M. White-Sand Savannas Expand at the Core of the Amazon After Forest Wildfires. *Ecosystems* **24**, 1624–1637 (2021).

16. Donovan, V. M., Wonkka, C. L. & Twidwell, D. Surging wildfire activity in a grassland biome. *Geophys. Res. Lett.* **44**, 5986–5993 (2017).

17. Milliman, J. D. & Meade, R. H. World wide delivery of river sediments to the oceans.

J. Geol. **91**, 1–21 (1983).

18. Galy, V. *et al.* Efficient organic carbon burial in the Bengal fan sustained by the Himalayan erosional system. *Nature* **450**, 407–410 (2007).

19. Freeman, K. H. & Colarusso, L. A. Molecular and isotopic records of C4 grassland expansion in the late miocene. *Geochim. Cosmochim. Acta* **65**, 1439–1454 (2001).

20. McNeill, L. C. *et al.* Understanding Himalayan erosion and the significance of the Nicobar Fan. *Earth Planet. Sci. Lett.* **475**, 134–142 (2017).

21. Chen, W. H. *et al.* Drainage evolution and exhumation history of the eastern Himalaya: Insights from the Nicobar Fan, northeastern Indian Ocean. *Earth Planet. Sci. Lett.* **548**, 116472 (2020).

22. Pickering, K. T. *et al.* Sedimentology, stratigraphy and architecture of the Nicobar Fan (Bengal–Nicobar Fan System), Indian Ocean: Results from International Ocean Discovery Program Expedition 362. *Sedimentology* **67**, 2248–2281 (2020).

23. Mcneill, L., Dugan, B., Petronotis, K., Milliken, K. & Francis, J. Late Miocene wood recovered in Bengal-Nicobar submarine fan sediments by IODP Expedition 362. *Sci. Drill.* **27**, 49–52 (2020).

24. McNeill, L. C. *et al.* Site U1480. In McNeill, L.C., Dugan, B., Petronotis, K.E., and the Expedition 362 Scientists, Sumatra Subduction Zone. *Proc. Int. Ocean Discov. Program, 362 Coll. Station. TX (International Ocean Discov. Program)* (2017) doi:https://doi.org/10.14379/iodp.proc.362.103.2017.

25. Basu, S. *et al.* Carbon isotopic ratios of modern C3-C4 plants from the Gangetic Plain, India and its implications to paleovegetational reconstruction. *Palaeogeogr. Palaeoclimatol. Palaeoecol.* **440**, 22–32 (2015).

290 26. Zin-Maung-Maung-Thein *et al.* Stable isotope analysis of the tooth enamel of
291 Chaingzauk mammalian fauna (late Neogene, Myanmar) and its implication to
292 paleoenvironment and paleogeography. *Palaeogeogr. Palaeoclimatol. Palaeoecol.*
293 **300**, 11–22 (2011).

294 27. Srivastava, G., Paudayal, K. N., Utescher, T. & Mehrotra, R. C. Miocene vegetation
295 shift and climate change: Evidence from the Siwalik of Nepal. *Glob. Planet. Change*
296 **161**, 108–120 (2018).

297 28. Ehleringer, J. R., Cerling, T. E. & Brent R. Helliker. C4 photosynthesis, atmospheric
298 CO2, and climate. *Oecologia* **112**, 285–299 (1997).

299 29. Pagani, M., Arthur, M. A. & Freeman, K. H. Miocene evolution of atmospheric carbon
300 dioxide. *Paleoceanography* **14**, 273–292 (1999).

301 30. Sage, R. F. The evolution of C4 photosynthesis. *New Phytol.* **161**, 341–370 (2004).

302 31. Polissar, P. J., Rose, C., Uno, K. T., Phelps, S. R. & deMenocal, P. Synchronous rise
303 of African C4 ecosystems 10 million years ago in the absence of aridification. *Nat.*
304 *Geosci.* **12**, 657–660 (2019).

305 32. Yue, X. & Unger, N. Fire air pollution reduces global terrestrial productivity. *Nat.*
306 *Commun.* **9**, (2018).

307 33. Vitousek, P. M. *et al.* Nitrate losses from disturbed ecosystems. *Science (80-.).* **204**,
308 469–474 (1979).

309 34. Denk, T. R. A. *et al.* The nitrogen cycle: A review of isotope effects and isotope
310 modeling approaches. *Soil Biol. Biochem.* **105**, 121–137 (2017).

311 35. Nommik, H. Fixation and biological availability of ammonium in soil clay minerals.
312 *Ecol. Bull.* 273–279 (1981).

313 36. Herman, D. J. & Rundel, P. W. Nitrogen Isotope Fractionation in Burned and
314 Unburned Chaparral Soils. *Soil Sci. Soc. Am. J.* **53**, 1229–1236 (1989).

315 37. Turner, M. G., Smithwick, E. A. H., Metzger, K. L., Tinker, D. B. & Romme, W. H.
316 Inorganic nitrogen availability after severe stand-replacing fire in the Greater
317 Yellowstone ecosystem. *Proc. Natl. Acad. Sci. U. S. A.* **104**, 4782–4789 (2007).

318 38. Vitousek, P. M. & Melillo, J. M. Nitrate Losses From Disturbed Forests: Patterns and
319 Mechanisms. *For. Sci.* **25**, 605–619 (1979).

320 39. Hart, S. C., DeLuca, T. H., Newman, G. S., MacKenzie, M. D. & Boyle, S. I. Post-fire
321 vegetative dynamics as drivers of microbial community structure and function in forest
322 soils. *For. Ecol. Manage.* **220**, 166–184 (2005).

323 40. Zakir Hossain, H. M., Sampei, Y. & Roser, B. P. Polycyclic aromatic hydrocarbons
324 (PAHs) in late Eocene to early Pleistocene mudstones of the Sylhet succession, NE
325 Bengal Basin, Bangladesh: Implications for source and paleoclimate conditions during
326 Himalayan uplift. *Org. Geochem.* **56**, 25–39 (2013).

327 41. Fletcher, T. L. *et al.* Evidence for fire in the pliocene arctic in response to amplified
328 temperature. *Clim. Past* **15**, 1063–1081 (2019).

329 42. Melott, A. L. & Thomas, B. C. Geological note from cosmic explosions to terrestrial
330 fires? *J. Geol.* **127**, 475–482 (2019).

331 43. Dobriyal, M. J. & Bijalwan, A. Forest fire in western Himalayas of India: A Review.
332 *New York Sci. J. 2017;10(6)* **10**, 39–46 (2017).

333 44. Wallner, A. *et al.* 60Fe and 244Pu deposited on Earth constrain the r-process yields of
334 recent nearby supernovae. *Science (80-.).* **372**, 742–745 (2021).

335 45. Müller, P. J. C/N ratios in Pacific deep-sea sediments: Effect of inorganic ammonium

and organic nitrogen compounds sorbed by clays. *Geochim. Cosmochim. Acta* **41**, 765–776 (1977).

46. Schildgen, T. F., Van Der Beek, P. A., Sinclair, H. D. & Thiede, R. C. Spatial correlation bias in late-Cenozoic erosion histories derived from thermochronology. *Nature* **559**, 89–93 (2018).

47. Subbarao, K. V. & Hedge, C. E. K, Rb, Sr and 87Sr86Sr in rocks from the Mid-Indian Oceanic Ridge. *Earth Planet. Sci. Lett.* **18**, 223–228 (1973).

48. Richter, F. M., Rowley, D. B. & DePaolo, D. J. Sr isotope evolution of seawater: the role of tectonics. *Earth Planet. Sci. Lett.* **109**, 11–23 (1992).

49. Willenbring, J. K. & Von Blanckenburg, F. Long-term stability of global erosion rates and weathering during late-Cenozoic cooling. *Nature* **465**, 211–214 (2010).

50. Derry, L. A. & France-Lanord, C. Neogene Himalayan weathering history and river 87Sr/86Sr: Impact on the marine Sr record. *Earth Planet. Sci. Lett.* **142**, 59–74 (1996).

51. Quade, J., Roe, L., DeCelles, P. G. & Ojha, T. P. The late neogene 87Sr/86Sr record of lowland himalayan rivers. *Science (80-.).* **276**, 1828–1831 (1997).

52. Harris, N. Significance of weathering Himalayan metasedimentary rocks and leucogranites for the Sr isotope evolution of seawater during the early Miocene. 795–798 (1995).

53. Seki, O. *et al.* Alkenone and boron-based Pliocene pCO2 records. *Earth Planet. Sci. Lett.* **292**, 201–211 (2010).

54. Bartoli, G., Hönisch, B. & Zeebe, R. E. Atmospheric CO2 decline during the Pliocene intensification of Northern Hemisphere glaciations. *Paleoceanography* **26**, 1–14 (2011).

359 55. Sosdian, S. M. *et al.* Constraining the evolution of Neogene ocean carbonate chemistry
360 using the boron isotope pH proxy. *Earth Planet. Sci. Lett.* **498**, 362–376 (2018).

361 56. Kaushal, R. & Ghosh, P. Stable Oxygen and Carbon Isotopic Composition of Rice
362 (Oryza sativa L.) Grains as Recorder of Relative Humidity. *J. Geophys. Res.*
363 *Biogeosciences* **123**, 423–439 (2018).

364 57. McNeill, L. C. *et al.* IODP Expedition 362 Bulk and grain density (MAD). (2020)
365 doi:10.5281/ZENODO.3754978.

366 58. SilvaJ.A & Bremner, J. M. Determination and isotope-ratio analysis of different forms
367 of nitrogen in soils: 5. Fixed Ammonium. *Soil Sci. Soc. Am. J.* **30**, 587–594 (1966).

368 59. Petit, S., Righi, D. & Madejová, J. Infrared spectroscopy of NH4+-bearing and
369 saturated clay minerals: A review of the study of layer charge. *Appl. Clay Sci.* **34**, 22–
370 30 (2006).

371 60. Petit, S., Righi, D., Madejová, J. & Decarreau, A. Interpretation of the infrared
372 spectrum of the -clays: application to the evaluation of the layer charge. *Clay Miner.*
373 **34**, 543–549 (1999).

374 61. Pironon, J. ., Pelletier, M., De Donato, P. & Mosser-Ruck, R. Characterization of
375 smectite and illite by FTIR spectroscopy of interlayer NH 4 + cations . *Clay Miner.* **38**,
376 201–211 (2003).

377 62. McNeill, L. C. *et al.* IODP Expedition 362 Magnetic susceptibility (whole round).
378 (2020) doi:10.5281/ZENODO.3754959.

379 63. Charreau, J. *et al.* Paleo-erosion rates in Central Asia since 9Ma: A transient increase
380 at the onset of Quaternary glaciations? *Earth Planet. Sci. Lett.* **304**, 85–92 (2011).

381 64. Farrell, J. W., Clemens, S. C. & Gromet, L. P. Improved chronostratigraphic reference

curve of late Neogene seawater 87 Sr/ 86 Sr. *Geology* **23**, 403–406 (1995).

65. Beets, C. J. The late Neogene 87Sr/86Sr isotopic record in the western Arabian Sea, Site 722. *Prell, WL; Niitsuma, N; al. (eds.), Proc. Ocean Drill. Program, Sci. Results, Coll. Station. TX (Ocean Drill. Program)* **117**, 459–463 (1991).

66. Matsui, H. *et al.* Integrated Neogene biochemostratigraphy at DSDP Site 296 on the Kyushu-Palau Ridge in the western North Pacific. *Newsletters Stratigr.* **53**, 313–331 (2020).

67. Hodell, D. A., Mead, G. A. & Mueller, P. A. Variation in the strontium isotopic composition of seawater (8 Ma to present) : Implications for chemical weathering rates and dissolved fluxes to the oceans. *Chem. Geol. Isot. Geosci. Sect.* **80**, 291–307 (1990).

68. Hodell, D. A., Mueller, P. A., McKenzie, J. A. & Mead, G. A. Strontium isotope stratigraphy and geochemistry of the late Neogene ocean. *Earth Planet. Sci. Lett.* **92**, 165–178 (1989).

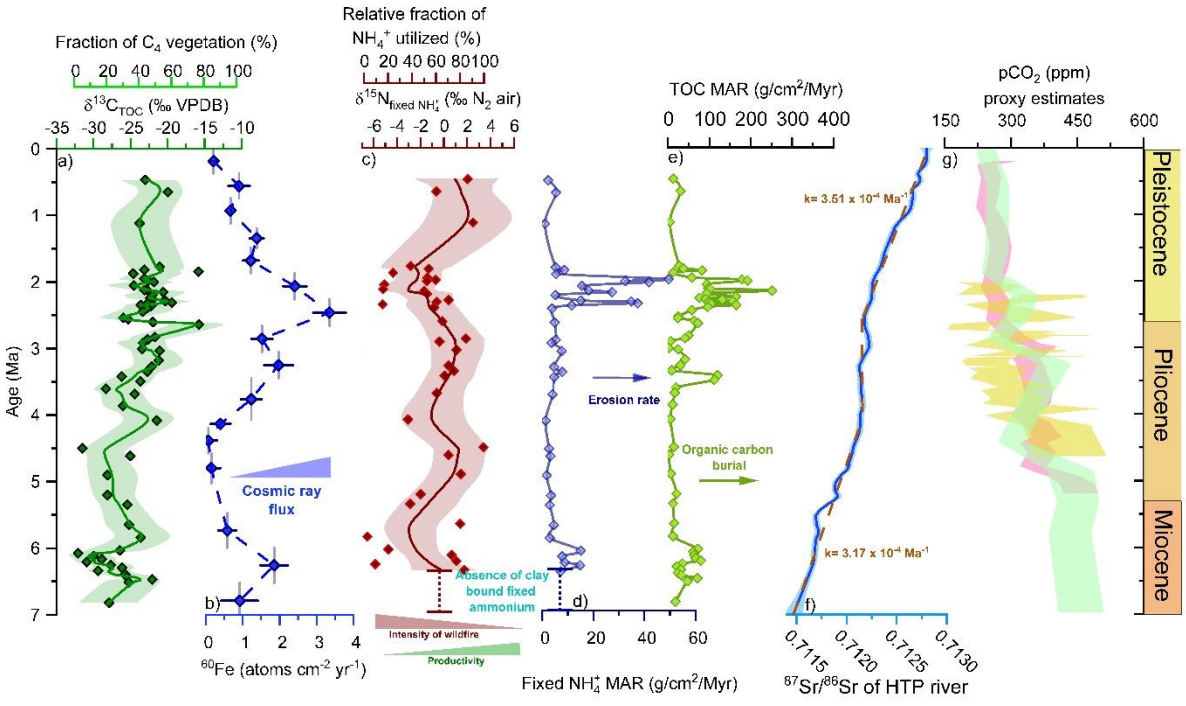

Fig. 1: C_4 vegetation and Wildfire impact on CO_2 drawdown during Late Cenozoic. a, $\delta^{13}C_{TOC}$ and estimated fraction of C_4 vegetation (%). **b,** Decay corrected ^{60}Fe incorporation rate as a proxy of cosmic ray flux from nearby supernova explosion[44]. **c,** $\delta^{15}N_{\text{fixed NH4+}}$ and estimated relative fraction of nutrient (NH_4^+) utilization as a proxy of wildfire intensity. **d,** Fixed NH_4^+ MAR as a proxy for erosion rate. **e,** TOC MAR as a proxy of the burial of organic carbon. **f,** Reconstructed $^{87}Sr/^{86}Sr$ ratio of Himalayan Tibetan Plateau(HTP) river and reaction rate (k) between 7 Ma to 4 Ma and 2.5 Ma to the modern-day. **g,** Alkenone (Pink)[53] and Boron isotope of foraminifera (Yellow[54] & Green[55]) based pCO_2 reconstruction. The solid line and shaded area in panels a,c, and f indicate the LOESS fit line and 95% confidence interval, respectively, computed using the R language SpaitalEco package.

Methods:

Stable isotope of Total Organic Carbon and TOC MAR:

Total 64 samples were selected from Unit I and Unit II of IODP-362 site U1480 based on the yield of organic matter. Prior to isotope analysis, the samples were decarbonated with 1N HCl at room temperature. After ensuring the complete removal of carbonate, the samples were rinsed with Milli-Q water until pH attain neutral. These samples were dried in a hot air oven at 70°C for a minimum duration of 24 hours and homogenized using agate mortar and pestle. Around 5mg of these samples were packed in tin capsule and combusted at 850°C in the Flash 2000 Elemental Analyser that was coupled with Delta V advantage IRMS (by Thermo Electron Corporation, Bremen) interfaced via CONFLO IV. Carbon isotopic compositions are reported in the conventional delta notation (δ) in per mill (‰) relative to Vienna Pee Dee Belemnite (VPDB). The lab working reference materials, which includes OASIS_Glucose ($\delta^{13}C = -10.99$ ‰VPDB) and OASIS_Rice ($\delta^{13}C = -27.67$ ‰VPDB) were assigned isotope value analyzing with IAEA secondary reference material; IAEA-CH-6[56]. Further any drift in analytical results was ascertained with analysis of reference material for multiple times in a batch at regular intervals after analysis of every 3-4 samples. This allows assignment of δ-values to the samples using standard-sample bracketing methodology. The standard deviation of $\delta^{13}C$ for OASIS_Glucose (n=17) and OASIS_Rice (n=13) are 0.07‰ and 0.1‰, respectively.

For estimating the weight percentage of organic carbon, we calibrated our analysis with OASIS_Glucose varying the amount ranging between 100 to 500µg in a batch. A linear regression relationship between amount of carbon in OASIS Glucose (from the mass of glucose* 0.4) and total peak area (peak area of ^{12}C and peak area of ^{13}C) to determine the TOC % in the sample [(mass of carbon in the sample/ total mass of sample) * 100%]. Further, TOC Mass Accumulation Rate (TOC MAR) was obtained from dry bulk density of sediment, sedimentation rate and TOC content (DBD* Sed Rate* TOC %/100) where Dry Bulk Density (DBD) followed previously in other studies[20,57].

Clay bound ammonium stable isotope and fixed NH_4^+ MAR:

For stable isotope and weight percentage analysis of fixed NH_4^+ in clay, we treated the 500-1000mg clay fraction of 38 samples from Unit I and Unit II of IODP-362 site U1480 with 20 ml of KOBr-KOH solution to eliminate the organic nitrogen fraction[58]. The KOBr-KOH solution was concocted by adding 6 ml bromine solution at 0.5 ml/min to 200 ml of 2 M KOH cooled in the ice bath. After adding the KOBr-KOH solution with clay, the beaker was swirled and allowed to stand for 2 hours with the beaker mouth covered by watch glass. Then, 60ml of milli-Q water was added in the beaker and the mixture was boiled strenuously for 5 minutes. After that the mixture cooled overnight and decanted and discarded the supernatant liquid. To remove exchangeable ammonium, the residue was treated with 0.5M KCl. The high concentration of potassium in the solution during the whole process prevents the adsorption by clay minerals of ammonium formed during the oxidation process. Finally, the sample was brought to neutral pH by rinsing with milli-Q water and dried in hot-air over at 70°C for a duration of 24 hours.

Around 50 to 100 mg of dried clay was packed in tin capsule and combusted at 850°C in the Flash 2000 Elemental Analyser that was coupled with Delta V advantage IRMS (by Thermo Electron Corporation, Bremen) interfaced via CONFLO IV. Nitrogen isotopic compositions are reported in the conventional delta notation (δ) in per mill (‰) relative to N_2 air. IAEA_NO3 ($\delta^{15}N$ = 4.7‰ N_2 air) standard was run between 4-5 samples to correct for isotopic drift during a batch and to assign δ-value for samples using standard-sample bracketing method. The analytical precision $\delta^{15}N$ based on replicate analysis of Merck Sodium nitrate is 0.2‰ (n=10).

For estimating the weight percentage of fixed NH_4^+ in clay, we loaded the IAEA_NO3 with amount ranges between 200 to 500µg in each batch of analysis. We then used the linear regression relationship between amount of nitrogen in IAEA_NO3 (mass of glucose* 0.139) and total peak area (peak area of ^{14}N and peak area of ^{15}N) to estimate sample fixed NH_4^+ % [(mass of nitrogen in the sample/ total mass of sample) * 1.29* 100%]. Then, We calculated fixed NH_4^+ Mass Accumulation Rate (fixed NH_4^+ MAR) as (DBD* Sed Rate* fixed NH_4^+ %/100) where Dry Bulk Density (DBD) and Sedimentation Rate were obtained from McNeill et al.,[57] and [20], respectively.

As shown by Silva and Bremner[58], the efficiency of the method for removing the organic nitrogen fraction (hydrolyzable and nonhydrolyzable organic nitrogen) is higher than 98%. Additionally, we checked the efficiency of the oxidation of proteinaceous material (Peptone) by determining the total N content of the peptone before and after the KOBr-KOH treatment. The N content value for KOBr-KOH treated peptone is below the detection limit.

FT-IR analysis of clay fraction of sample:

FT-IR spectra for the clay fraction sample after organic matter removal by KOBr-KCl treatment are shown in Extended Data Fig 2. All spectrums were measured under the reflectance mode using Spectragryph ver.1.2.6 software and converted into absorbance mode to validate with library. The weak absorption of NH_4^+ was detected at around 1280-1600 cm^{-1} within NH_4^+ bend region[59]. Also, the very tiny to weak N-H stretching absorption was detected within 3100-3430 cm^{-1} [59–61]. The trace levels of absorption within the NH_4^+ region suggest that the mineralized nitrogen in the clay fraction is possibly ammonium fixed in the interlayers of clay mineral.

Acknowledgment:

This research used samples provided by the IODP Expedition 362. We thank the Co-Chief's, Program Scientist and other shipboard members from the scientific and technical team on board JOIDES Resolution during IODP-362 drilling. This research is financially funded by IODP-India at National Centre for Polar and Ocean Research, Goa (Ministry of Earth Sciences, India) through Grant No: NCAOR/IODP/20.25/2018(2). TS thanks Council of Scientific and

Industrial Research, Government of India for the financial support in the form of fellowship for PhD (File No.: 09/079 (2811)/2019-EMR-1) and Divecha Centre for Climate Change, IISc, India for Grantham fellowship. We also thank Dhananjai Pandey for the discussion and Dimple Rani for helping in the FTIR analysis.

Author contributions: PG and TS conceptualize the problem; PG and NN generated fund for the project. TS analysed the samples and wrote the paper along with PG. NN provided the samples and involved in the discussion.

Declaration of Competing Interest:

Authors declare that they have no competing interests.

Data and materials availability:

All data needed to evaluate the conclusions in the paper are present in the paper and/or the Supplementary Materials. Additional data related to this paper may be requested from the authors.

Extended Data Fig 1: Multiple evidence of increased erosion rate during late Miocene and Plio-Pleistocene boundary

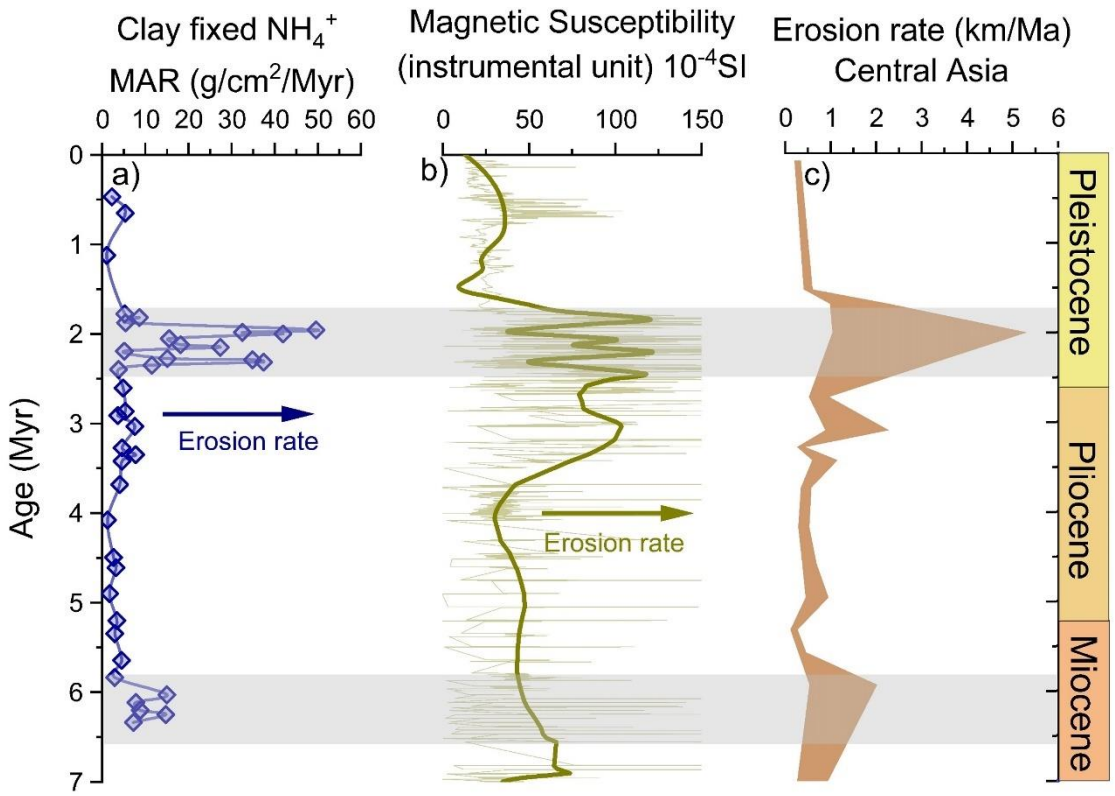

a) Fixed NH_4^+ MAR from IODP site U1480 (present study). b) Magnetic susceptibility from IODP site U1480[62]. c) cosmogenic ^{10}Be concentrations based erosion rate from central Asia[63].

Extended Data Fig 2: Representative FT-IR spectra of the clay fraction of sample from Late Pliocene section of IODP 362 after KOBr-KCl treatment.

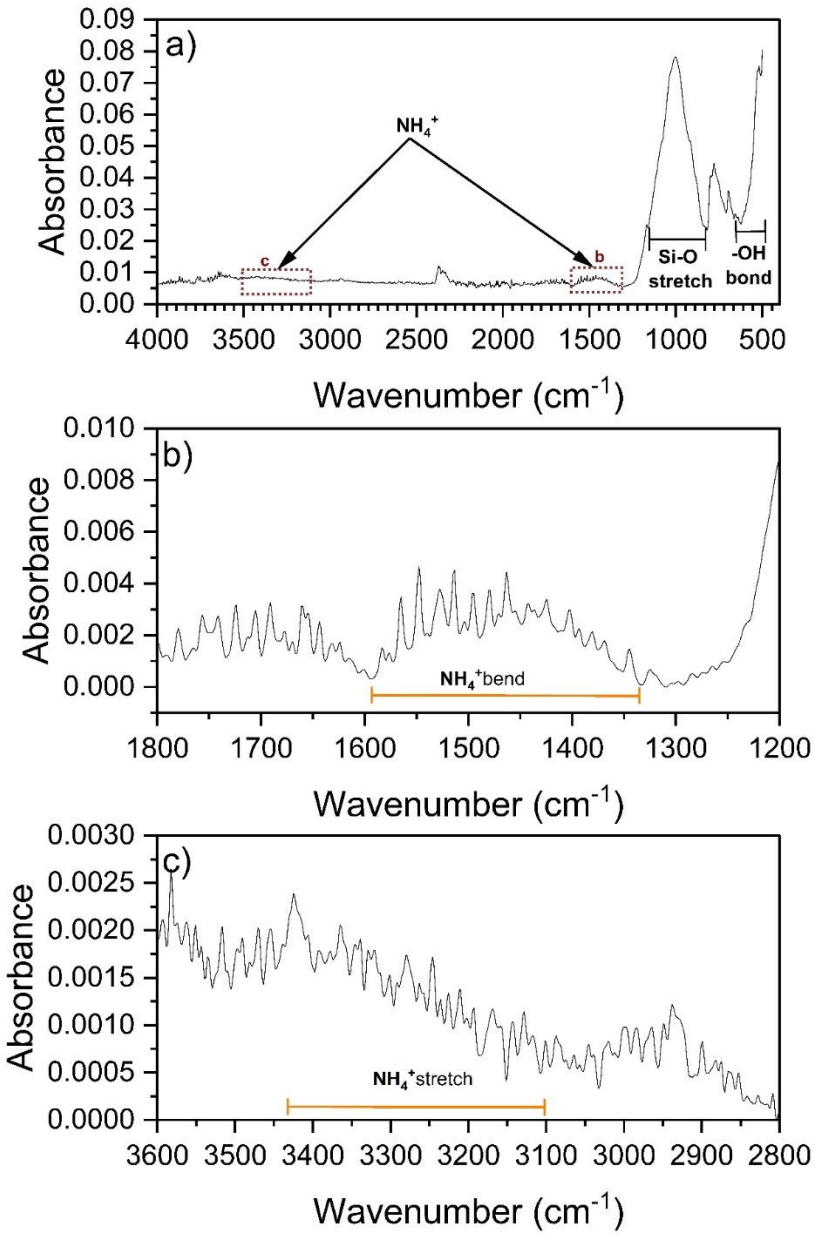

a) OH- bond, Si-O stretch, NH_4^+ absorption peak was shown in the absorbance band from 400 to 4000 cm^{-1} wavenumber; b) Absorbance band of NH_4^+ bend; c) Absorbance band of NH_4^+ stretch.

Extended Data Fig. 3: Late Cenozoic evolution of global seawater $^{87}Sr/^{86}Sr$ ratio.

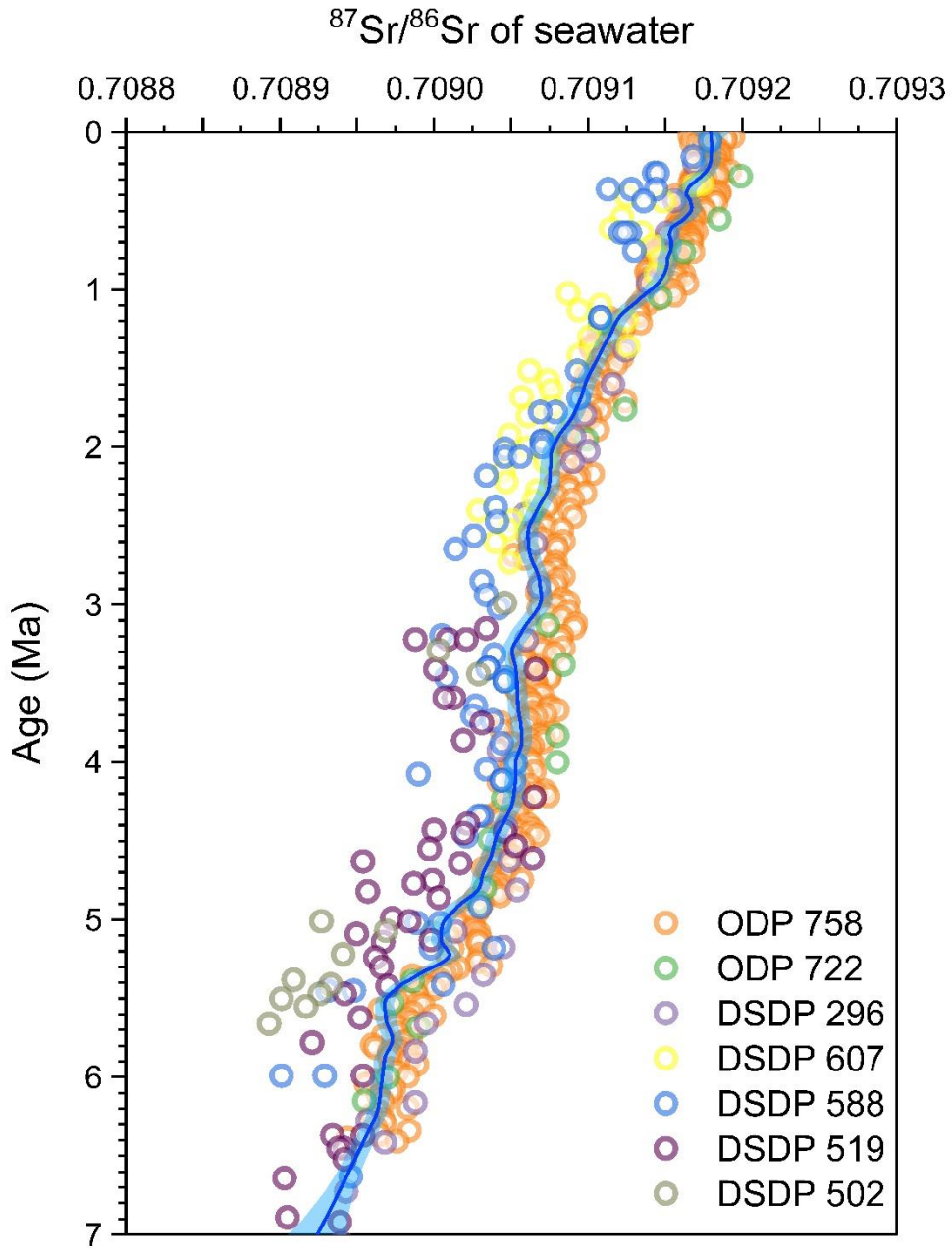

Compilation of $^{87}Sr/^{86}Sr$ marine authigenic carbonate from ODP[64,65] and DSDP[66–68] sites. The solid blue line and shaded area indicate the LOESS fit line and 95% confidence interval computed using the R language SpaitalEco package.

Supplementary Files

This is a list of supplementary files associated with this preprint. Click to download.

- Extendeddatatable1.xlsx
- Extendeddatatable2.xlsx